Electronic Supplementary Material (ESI) for Nanoscale.

Supporting Information for

Tunable black phosphorus heterojunction transistor for multifunctional optoelectronics

Lin Wang, Li Huang, Wee Chong Tan, Xuewei Feng, Li Chen, Kah Wee Ang*

Department of Electrical and Computer Engineering, National University of Singapore, 4 Engineering Drive 3, Singapore

Centre for Advanced 2D Materials, National University of Singapore, 6 Science Drive 2, Singapore

E-mail: eleakw@nus.edu.sg

Section 1. Raman spectrum of BP flake for heterojunction device fabrication.

Section 2. Transfer characteristics of BP heterojunction transistors D2 and D3.

Section 3. I_d-V_g characteristics and V_{th} shift of D1 under various illumination situations.

Section 4. Photoresponse of BP heterojunction phototransistor D1 operating at 1 V V_d.

Section 5. Photodetection results on BP heterojunction phototransistor D2.

Section 6. Photodetection results on BP heterojunction phototransistor D3.

Section 7. Detailed comparison of infrared responsivity of BP heterojunction phototransistor with reported values.

Section 8. Calculation of NEP and D^*.

Section 9. Carrier lifetime and band width analysis of D1.

Section 10. Photoresponse of the device in dependence of V_d.

Section 11. Source/drain contact nature of the device and explanation of gate-dependent rectifying behavior.

Section 12. Zero-power-consumption infrared photodetection with D2 and D3. (Indicating potential of heterostructure design for improved optoelectronic performance)

Section 1. Raman spectrum of BP flake for heterojunction device fabrication.

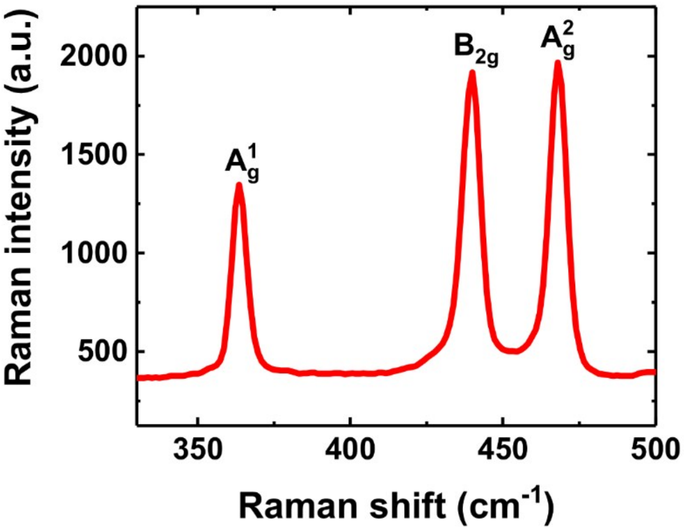

Figure S1. Raman spectrum of the BP flake used for device fabrication. Three peaks are identified at 363.5 cm^{-1}, 439.9 cm^{-1} and 467.9 cm^{-1}, corresponding to A_g^1, B_{2g} $and\ A_g^2$ phonon mode, respectively, confirming the good crystal quality of the BP flake.

Section 2. Transfer characteristics of BP heterojunction transistors D2 and D3.

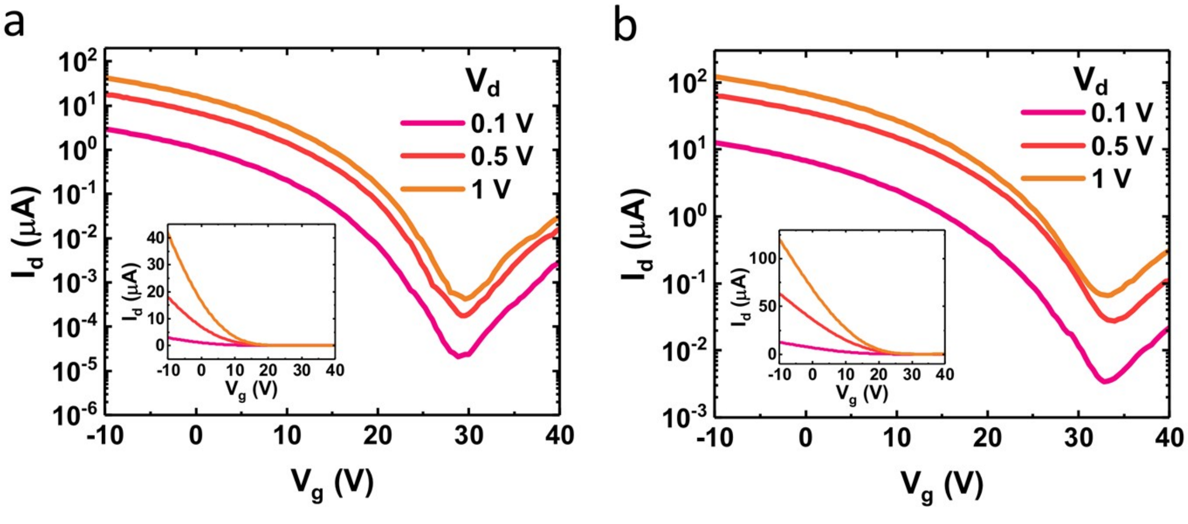

Figure S2. Transfer characteristics of device (a) D2 and (b) D3 on semi-logarithmic scale and linear scale (inset) at different V_d biases, showing hole-dominating conduction, similar to device D1.

Section 3. I_d-V_g characteristics and V_{th} shift of D1 under various illumination situations.

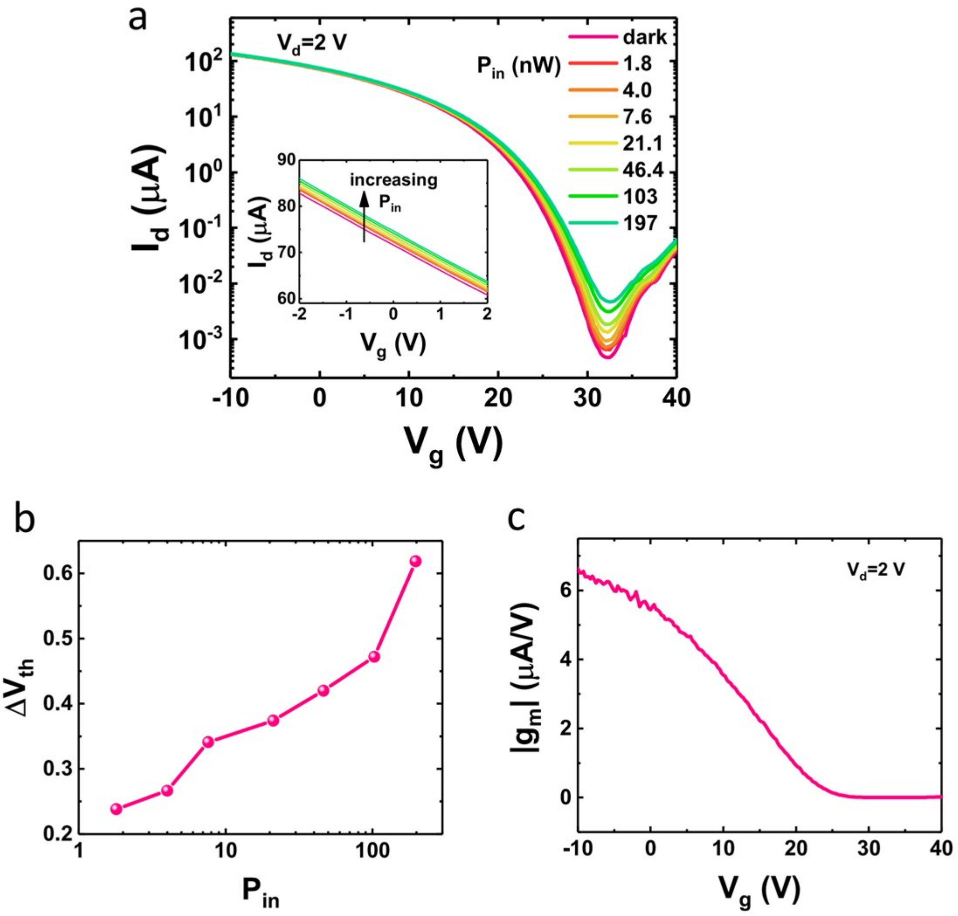

Figure S3. (a) I_d-V_g characteristics of the device D1 under varying illumination situations at 1550 nm and at 2 V V_d. Inset shows the portion near V_g=0 V on linear scale. (b) Extracted threshold voltage (V_{th}) shift as a function of incident light power. (c) Transconductance curve of D1 at 2 V V_d.

Section 4. Photoresponse of BP heterojunction phototransistor D1 operating at 1 V V_d.

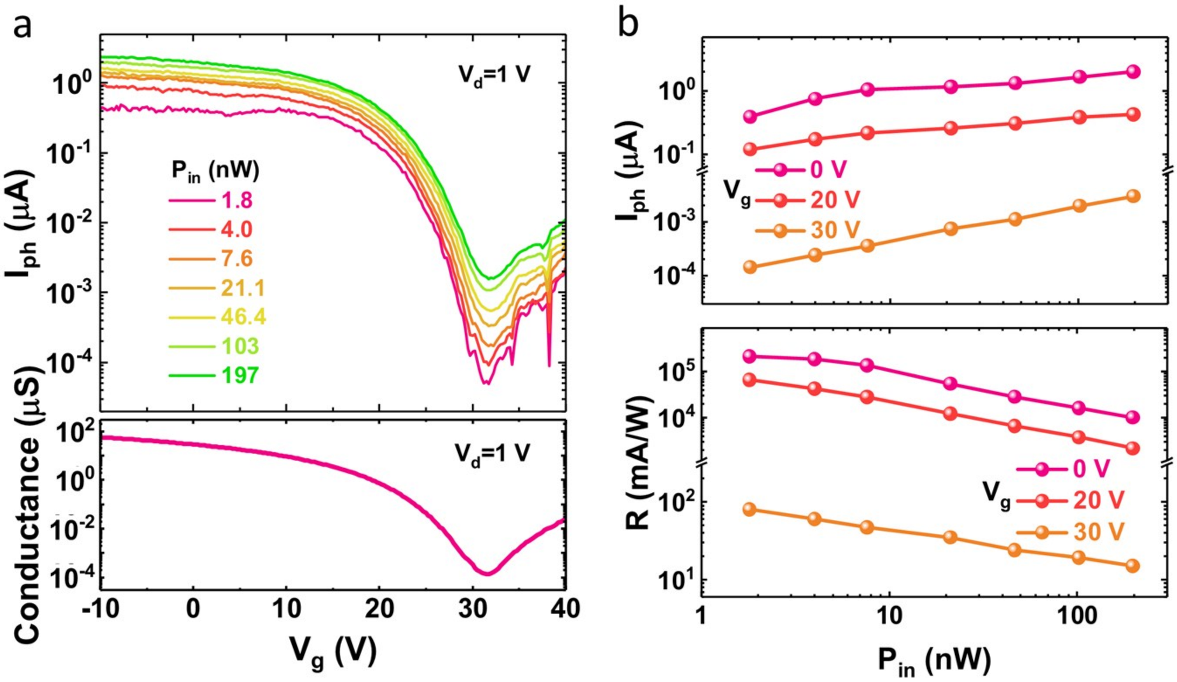

Figure S4. Tunable photoresponse of lateral BP heterojunction phototransistor D1 under 1 V V_d bias at 1550 nm wavelength. (a) Bottom panel: Conductance of the device as a function of V_g under dark condition. Top panel: gate-bias-dependent photocurrent under varying light excitation power at 1 V V_d. (b) Top panel: Extracted photocurrent at typical V_g values (0 V, 20 V, 30 V, corresponding to on-state, subthreshold-state and off-state of the transistor) as a function of excitation light power. Bottom panel: Calculated photoresponsivity at typical V_g values and its dependence on light power. The highest responsivity is obtained to be 2.17×10^5 mA/W at 0 V V_g and 1.8 nW light power.

Section 5. Photodetection results on BP heterojunction phototransistor D2.

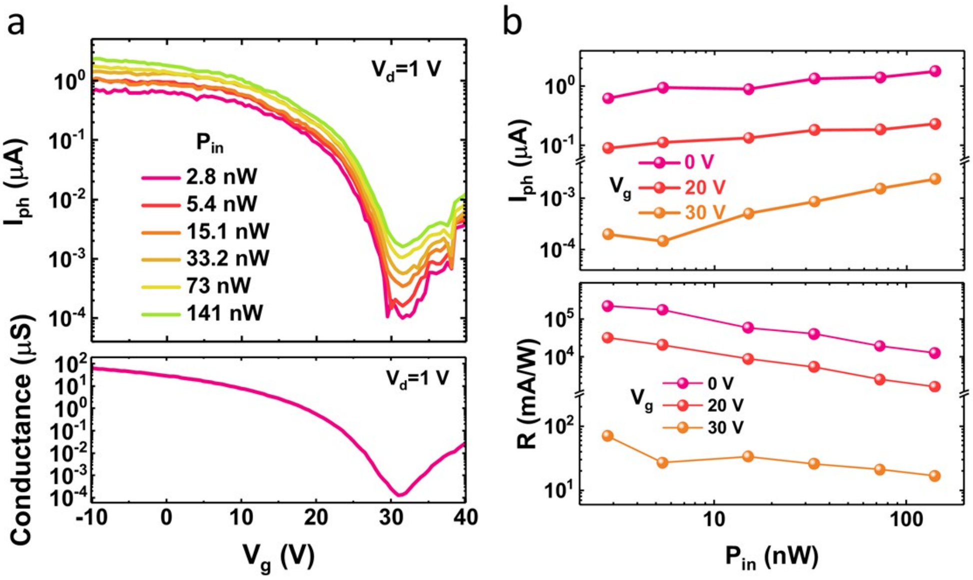

Figure S5. Tunable photoresponse of lateral BP heterojunction phototransistor D2 under 1 V V_d bias at 1550 nm wavelength. (a) Bottom panel: Conductance of the device as a function of V_g under dark condition. Top panel: gate-bias-dependent photocurrent under varying light excitation power at 1 V V_d. (b) Top panel: Extracted photocurrent at typical V_g values (0 V, 20 V, 30 V, corresponding to on-state, subthreshold-state and off-state of the transistor) as a function of excitation light power. Bottom panel: Calculated photoresponsivity at typical V_g values and its dependence on light power. The highest responsivity is obtained to be 2.23×10^5 mA/W at 0 V V_g and 2.8 nW light power.

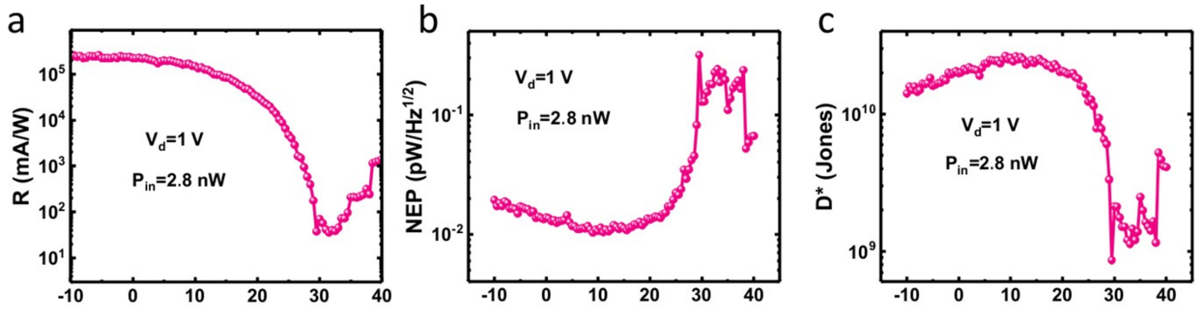

Figure S6. (a) Responsivity of lateral BP heterojunction phototransistor D2 as a function of V_g at 2.8 nW incident power at 1550 nm (V_d=1 V). (b) Noise-equivalent-power (NEP) of the device in dependence of V_g at 1 V V_d. The smallest NEP less than 10^{-2} pW/Hz$^{1/2}$ is obtained near 10 V gate bias. (d) Detectivity of the device in dependence of V_g at 1 V V_d. Value of 2.7×10^{10} Jones is obtained near 10 V V_g.

Section 6. Photodetection results on BP heterojunction phototransistor D3.

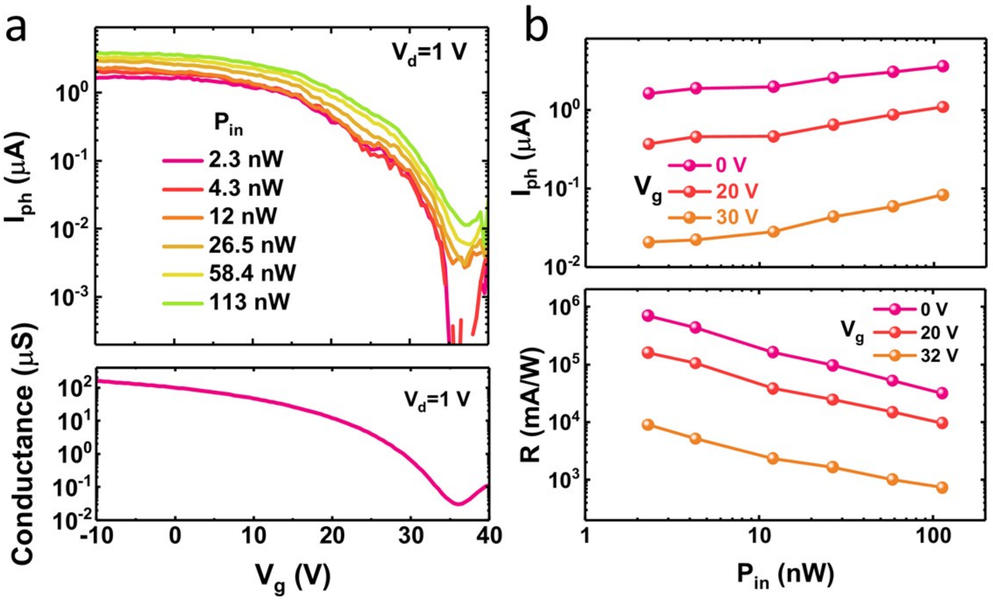

Figure S7. Tunable photoresponse of lateral BP heterojunction phototransistor D3 under 1 V V_d bias at 1550 nm wavelength. (a) Bottom panel: Conductance of the device as a function of V_g under dark condition. Top panel: gate-bias-dependent photocurrent under varying light excitation power at 1 V V_d. (b) Top panel: Extracted photocurrent at typical V_g values (0 V, 20 V, 32 V, corresponding to on-state, subthreshold-state, off-state of the transistor) as a function of excitation light power. Bottom panel: Calculated photoresponsivity at typical V_g values and its dependence on light power. The highest responsivity is obtained to be 7.01×10^5 mA/W at 0 V V_g and 2.3 nW light power. This higher responsivity value for device D3 (than D1 and D2) can be well attributed to more light absorption due to its larger BP thickness.

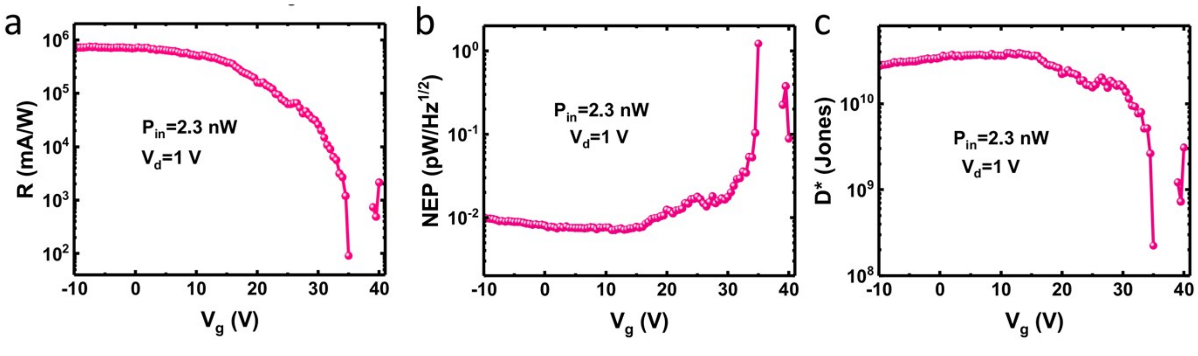

Figure S8. (a) Responsivity of lateral BP heterojunction phototransistor D3 as a function of V_g at 2.3 nW incident power at 1550 nm (V_d=1 V). (b) Noise-equivalent-power (NEP) of the device in dependence of V_g at 1 V V_d. The smallest NEP of 7×10^{-3} pW/Hz$^{1/2}$ is obtained near

15 V gate bias. (d) Detectivity of the device in dependence of V_g at 1 V V_d. A value of 3.8×10^{10} Jones is obtained near 15 V V_g.

Section 7. Detailed comparison of infrared responsivity of BP heterojunction phototransistor with reported values.

Table 1: Detailed comparison of photoresponsivity (R) between BP heterojunction device and reported BP-based photodetectors.

Structure	λ (nm)	R (mA/W)	BP thickness (nm)	$P_{in}/P_{density}$	V_d (V)	Reference in main text
BP heterojunction phototransistor	1550	383000	3-6	1.8 nW	2	**This work**
BP heterojunction phototransistor	1550	217000	3-6	1.8 nW	1	**This work**
waveguide-integrated phototransistor	1550	657 135	100 11.5	1.91 mW	0.4	[14]
phototransistor (interdigitated electrodes)	3390	82000	12	1.6 nW	0.5	[15]
phototransistor	2000	8500	23	10 nW	1	[17]
phototransistor	2500	47	15	25 µW	0.1	[18]
phototransistor	3700	21	15	25 µW	0.1	[18]
phototransistor	1550	5	120	3.1 kW/cm^2	0.2	[20]
phototransistor	1550	10000	20	82 µW	1.5	[21]
vertical BP junction	1200	0.35	30-50	1.35 mW	0.1	[26]
MoS_2/BP vertical junction	1550	153.4	12	1 nW	3	[27]
p-n junction	1470	180	2.5	50 W/cm^2	0.005	[28]
p-n junction	1064	120000	3	62.5 mW/cm^2	1	[36]
BP-on-WSe_2 phototransistor	1550	500	7	1 mW/cm^2	0.5	[37]

Section 8. Calculation of *NEP* and *D**.

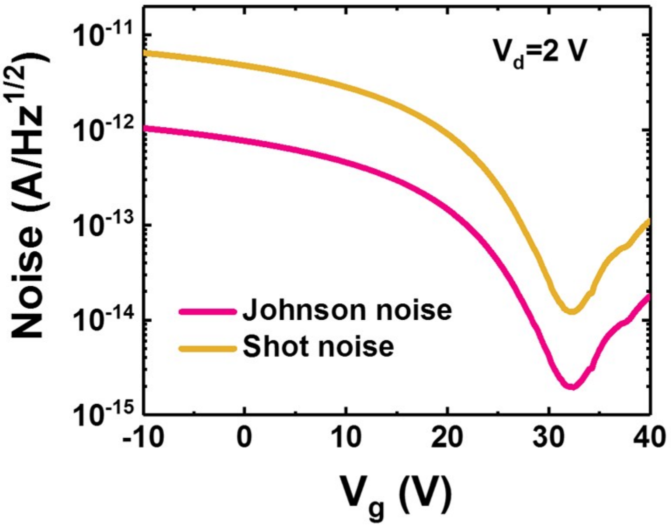

Figure S9. Calculated Johnson noise and shot noise of BP heterojunction transistor D1 as a function of V_g, showing shot noise being dominant over Johnson noise.

NEP indicates the excitation power needed to generate a signal equal to the device noise level in 1 Hz bandwidth and can be expressed by *NEP*=noise/*R*. Primarily, there are three contributions to the total noise: flicker noise, Johnson noise and shot noise. Among them, flicker noise are usually related to the defects acting as traps in the channel, and could be a dominating element in the total noise at low frequencies.[1] Johnson noise is caused by the thermal agitation of the charge carriers in the channel and can be expressed by $\sqrt{4k_BT\Delta f/R_{ch}}$ where k_B is the Boltzmann constant, *T* the temperature in Kelvin, and R_{ch} the channel resistance. Shot noise is related to the dark current and determined by $\sqrt{2qI_{dark}\Delta f}$. In our work, I_{dark} is recorded, and R_{ch} can be deduced by $R_{ch}=V_d/I_d$. Then, according to the above equations, the Johnson noise and shot noise of the device are calculated as a function of V_g for V_d=2 V. As shown in **Figure S9**, Johnson noise is almost one order of magnitude smaller than the shot noise. Therefore, the gate-dependent shot-noise-limited *NEP* of our device (NEP_{shot}) can be calculated as given in **Figure 3b**. Here, we would like to point out that at V_g=20 V (where lowest NEP_{shot} is obtained), our device can work at a relatively high frequency (4.2 kHz). Therefore, we believe that by combining with other advanced techniques, for example, lock-in technique at a high frequency of 4 kHz, it will be possible to avoid a large part of 1/*f* noise contribution and the NEP_{shot} will represent an ultimate limit of the device detection ability.

By the way, we would like to note that the calculated NEP_{shot} for V_g near 30 V is, although slightly higher than at 20 V V_g, still under 0.1 pW/Hz$^{1/2}$. In such case, since almost no traps contribute to the photocurrent generation (photoconductive effect dominates) and the device can work at a much higher frequency, it will be entirely possible to avoid $1/f$ noise on limiting the device *NEP* by employing lock-in technique. In this case, the NEP_{shot} represent the ultimate *NEP* of our device still is the smallest value compared to reported works.

Specific detectivity (D^*, in Jones) is an important figure of merit for photodetectors, which signifies the sensitivity of a photodetector normalized with its active area, thus can be used for comparison between different devices. It is given by $D^* = \sqrt{A}/NEP$, where A is the area of the detector in cm^2. For device D1, the channel length L=3.5 µm and channel width W=3 µm, resulting an area of 10.5 µm^2. Hence, the detectivity at V_g=0 V and V_g=20 V can be calculated to be 2.3×10^{10} Jones and 6.1×10^{10} Jones, respectively.

Section 9. Carrier lifetime and band width analysis.

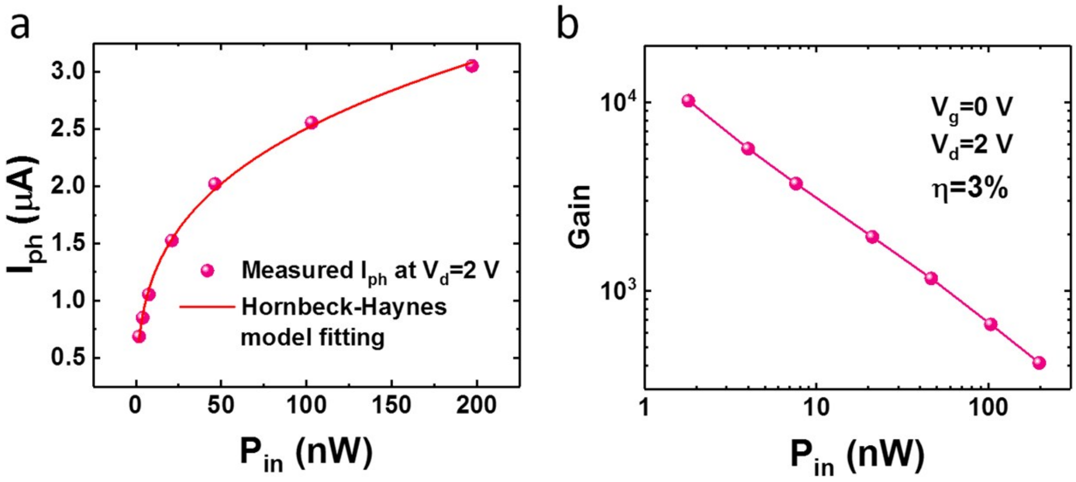

Figure S10. (a) Photocurrent (I_{ph}) as a function of incident laser power (P_{in}) at 0 V V_g and 2 V V_d, and the Hornbeck-Haynes model fitting for determining the carrier lift time. (b) Photoconductive gain of the device as a function of P_{in} when operating at 0 V V_g and 2 V V_d.

We adopt Hornbeck-Haynes model to describe the photocurrent dependence on the incident light power:[2]

$$I_{ph} = q\eta\frac{\tau_0}{\tau_{tr}}\frac{F}{1+(\frac{F}{F_0})^n},$$

where η is the absorption of BP channel, τ_0 and $\tau_{tr}=L^2/\mu_h V_d$ (L is the channel length, V_d is drain-source voltage, and μ_h is hole mobility) are the carrier lifetime and transit time, respectively, F is the photon absorption rate expressed by $F= \eta P_{in}/h\nu$ ($h\nu$ is the photon energy), F_0 is the absorption rate when trap saturation occurs, and n is a fitting parameter. According to the gain $G=(I_{ph}/P_{abs})(h\nu/q)$, where $P_{abs}=\eta P_{in}$ is the power absorbed by the channel, we have

$$G = \eta\frac{\tau_0}{\tau_{tr}}\frac{1}{1+(\frac{F}{F_0})^n}$$

For V_d=2 V and μ_h=100 cm^2/Vs, a carrier transit time of τ_{tr}=0.6 ns can be estimated. Regarding the absorption of our device, in ref[3], Zhang et al. has revealed absorption around 1%-3% for BP flake with 6 layers and 13 layers at 1550 nm (0.8 eV) wavelength. Therefore, we assume an absorption percentage of 3% of the incident light on the device for calculation, and a carrier lifetime of τ_0=39 μs is derived from the fitting results.

Consequently, the 3dB bandwidth $f_{3dB}=1/2\pi\tau_0$ is derived to be 4.2 kHz. Furthermore, when working at 30 V V_g, although a relatively smaller responsivity is obtained due to dominant photoconductive effect, the device frequency performance will be primarily determined by the carrier transit time (0.6 ns), implying its potential for GHz application.[4]

Section 10. Photoresponse of the device in dependence of V_d.

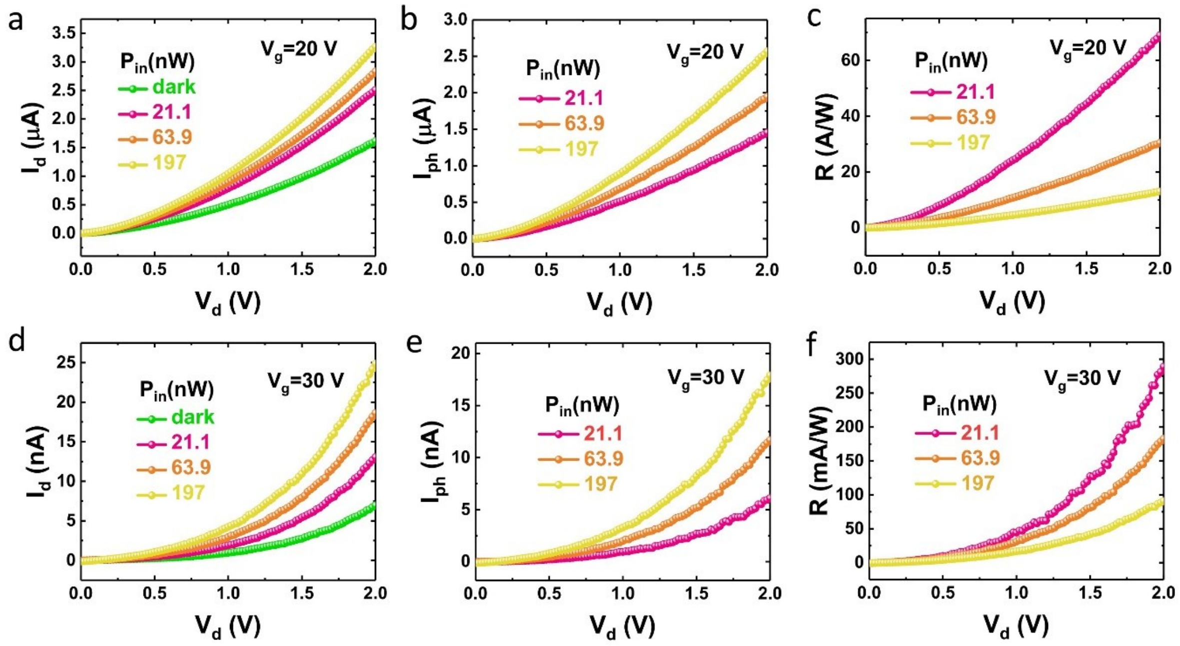

Figure S11. (a) I_d-V_d characteristics of the device under various illumination conditions at 20 V V_g. (b) Calculated photocurrent as a function of V_d at 20 V V_g. (c) Calculated responsivity as a function of V_d at 20 V V_g. (d) I_d-V_d characteristics of the device under various illumination conditions at 30 V V_g. (e) Calculated photocurrent as a function of V_d at 30 V V_g. (f) Calculated responsivity as a function of V_d at 30 V V_g. Moved to Supporting Information.

Section 11. Source/drain contact nature of the device and explanation of gate-dependent rectifying behavior

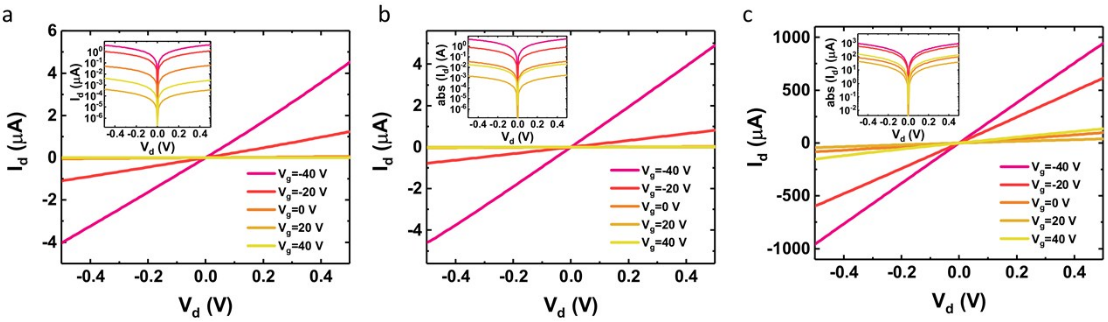

Figure S12. I_d-V_d characteristics at varying V_g values of devices on BP flakes of uniform thickness of (a) 3.5 nm, (b) 4.5 nm and (c) 7 nm. It is clear that these devices, which have similar flake thicknesses as in the BP heterojunction devices, display symmetric and linear I_d-V_d behaviours, indicating Ohmic-like nature of the Ni-electrode/BP contacts in this work. This fact implies that the metal/BP contact cannot explain the observed current rectification behavior of BP heterojunction device.

Therefore, concerning the gate-tunable rectifying behaviour in our BP device, it can be ascribed to the existence of a heterojunction between the thin and the thick portion in the channel, as a result of their distinct band gaps and different responses to the gate control. This rectifying behavior enables our device for photodetection at zero V_d, which is not allowed by other phototransistors with a homogeneous channel.

As for the V_g dependence, briefly, when V_g has a large enough negative value, both the regions (of different layer numbers) of the device are electrostatically modulated into heavy *p*-type forming a p^+-p^+ junction. Hence no significant rectifying phenomenon is expected at the thick-thin flake interface. Therefore the device shows no obvious current rectification. Regarding the evident rectifying behavior in the 10 to 30 V V_g range, it can be explained by the combined effect of the BP hetero-interface and BP/Ni contacts. First, the bands of the thin flake bend upwards at the interface due to its higher Fermi level (as a result of easier holes depletion and inversion) than the thick flake, which will induce a depletion region in the vicinity if the interface. Additionally, compared with the thick flake, the thin one has a larger band gap, and the valence band maximum is slightly lower than that for the thick flake. This will result in a slightly higher contact barrier at the source end, giving rise to a less effective injection of holes into the flake. Further increase of V_g results in degradation of rectifying behavior (rectifying ratio decreases) because the electron conduction is no longer negligible and electron injection is easier at the drain end. This can also help explain the reverse of rectifying direction when both flakes enter into the heavy electron doping regime.

Section 12. Zero-power-consumption infrared photodetection with D3. (Indicating potential of heterostructure design for improved optoelectronic performance)

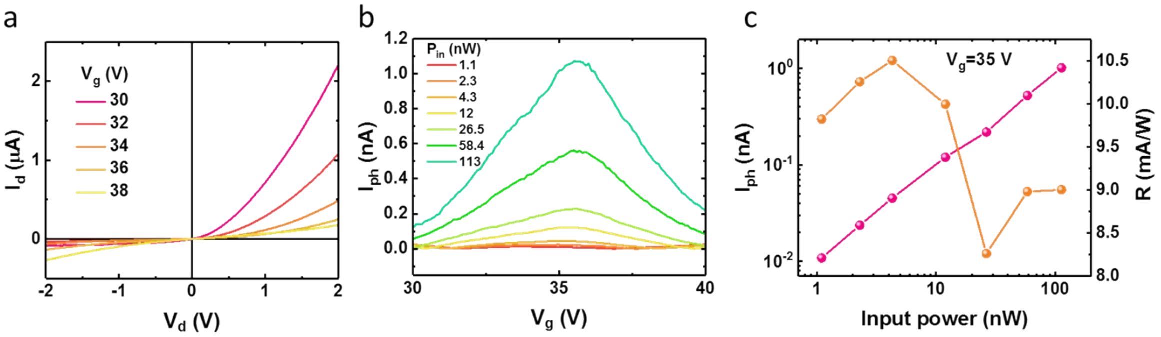

Figure S13. Zero-power-consumption infrared photodetection with D3. (a) I_d-V_d curves of the device for -2 V to 2 V V_d at different V_g showing current rectifying behavior. (b) Gate-tunable photocurrent arising from BP heterojunction transistor under varying laser powers with zero external V_d applied. (c) Extracted photocurrent (left axis) and photoresponsivity (right axis) in dependence of P_{in}. A maximized responsivity of 10.5 mA/W is obtained.

References

1 N. Clement, K.Nishiguchi, A. Fujiwara and D. Vuillaume, *Nat. Commun.* 2010**, 1**, 92.
2 C. Soci, A. Zhang, B. Xiang, S. A. Dayeh, D. P. Aplin, J. Park, X. Y. Bao, Y. H. Lo, D. Wang, Nano Lett. 2007, **7**, 1003.
3 G. Zhang, S. Huang, A. Chaves, C. Song, V. O. Ozcelik, T. Low and H. Yan , *Nat. Commun.* 2017**, 8**, 14071.
4 W. C. Tan, L. Huang, R. J. Ng, L. Wang, D. M. N. Hasan, T. J. Duffin, K. S. Kumar, C. A. Nijhuis, C. Lee, K. W. Ang, *Adv. Mater.* 2018, **30**, 1705039.